Feasibility Study of Line Integrated Backward Thomson Scattering Measurement in Nuclear Fusion Reactors

Yu-Ting LIN, Akira EJIRI, Kouji SHINOHARA, Yi PENG and Seowon JANG

The University of Tokyo, Kashiwa 277-8561, Japan

In order to control or suppress edge localized modes in nuclear fusion reactors, an accurate pedestal pressure profile measurement is necessary. A line integrated backward Thomson scattering measurement is an attractive method because of its long scattering length. Assuming that the first mirror is located far from the plasma to avoid degradation of the mirror due to erosion and impurity deposition, the measurement accuracies of density and temperature and pressure are estimated. For the target plasma, we adopt the pedestal profile with the shoulder density of 10^{19} - 10^{20} m^{-3} and the dimensions of the JA DEMO reactor. The calculation results show that, the Poisson noise due to finite detected scattered photon number is much larger than that due to bremsstrahlung emission. In addition, noise is enhanced by reconstruction process. The resultant total noise levels of reconstructed density, temperature and pressure profiles are at most 1.5%, 3%, 3%, respectively in the steep gradient region, and this method is feasible in the reactor.

1. Introduction

One of critical issues in nuclear fusion reactor diagnostics is the development of a measurement method of edge pedestal pressure profile. Due to the harsh environment and the required high reliability, a new measurement method should be developed. In this paper we present a feasibility study of edge pedestal electron temperature and density profile measurement using a line integrated backward Thomson scattering method.

The high confinement mode (H-mode) provides a necessary confinement regime for reactor scale tokamak fusion devices. In an H-mode, the edge steep pressure gradient often shows bursty edge instability called edge localized modes (ELMs) [1]. Particles and energy expelled by ELMs would significantly shorten the lifetime of the divertor plate. Therefore, ELM control or suppression is necessary for long pulse or steady state operation.

The stability of ELMs is determined by the pressure gradient driven ballooning mode and current driven peeling mode [2], which can be evaluated by measuring pedestal density and temperature profile. In ITER the required accuracy and the spatial resolution are 5%, 5 mm ($\Delta\psi_N \sim 0.04$) and 10%, 5 mm ($\Delta\psi_N \sim 0.04$) for density and temperature profiles, where ψ_N is normalized poloidal flux [3]. A Thomson scattering (TS) measurement is expected to satisfy these requirements in ITER, but it is believed to be difficult in fusion reactors because of the small solid angle of the first mirror. The first mirror should be located far from the plasma to avoid its degradation by high neutron flux and strong erosion and impurity deposition. In the study of EU DEMO, it is reported that the first mirror should be located behind a thin tube to avoid the degradation (Fig. 1). The ratio between the tube length (L) and the radius (r) should be over 50 [4] for visible light measurement. With such a tube the solid angle becomes very small ($\sim 1 \times 10^{-3}$ sr). Under this constraint, the standard edge Thomson scattering configuration with a horizontal laser beam and collection optics in an equatorial port [5] would show a poor performance as described later. In contrast, a line integrated backward Thomson scattering can have a long scattering length. In order to obtain spatial profile, however, the measurement with many integration chords is necessary to reconstruct the profiles. A LIDAR [6] is an attractive method, but the maximum spatial resolution can be achieved nowadays is ~ 70 mm [7], which is much larger than required spatial resolution. For LIDAR system with vertical laser beam, the required spatial resolution is relaxed, but it seems to be still smaller than achievable value as shown later.

In this paper, the feasibility of a line integrated backward Thomson scattering measurement is studied. A single lens model for estimating the sensitivity is described in Sec. 2. Estimation of line integrated Thomson scattering and background radiation signals are presented in Sec. 3. Reconstruction method of n_e, T_e profiles and their noise levels are shown in Sec. 4. Conclusions are given in Sec. 5.

author's e-mail: kevin850202@gmail.com

2. Concepts and Calculation Method

As the target device, we assume the JA DEMO reactor design [8]. The laser beam is injected from the upper port and the backward scattered light is collected by the first mirror located in the upper port. To satisfy the condition on the tube dimension [4], L and r are $L = 10$ m, $r = 0.2$ m, and the distance from the midplane to the tube entrance is 3 m (Fig. 1 (a)). Using a nearly vertical laser beam and an integration chord, a relatively long scattering length is expected. In the case of a standard horizontal laser beam configuration (Fig. 1 (b)), however, the maximum scattering length is limited by the required spatial resolution. Although a long scattering length ($\sim$ 1 m) is possible in the line integrated backward TS system, profile reconstruction is necessary, which may enhance the error, and we evaluate the errors including such an effect. In this paper, the profiles along the major radius are given as

$$n_e(R) = n_{e0} \times \left[\text{Tanh}(2(R_{gn} - R)/R_{wn}) + 1 \right]/2, \quad (1)$$

(a)

$L \sim 50r$

(b)

Vacuum vessel

Plasma

Laser beam

Collection optics — Fiber

Scattering length

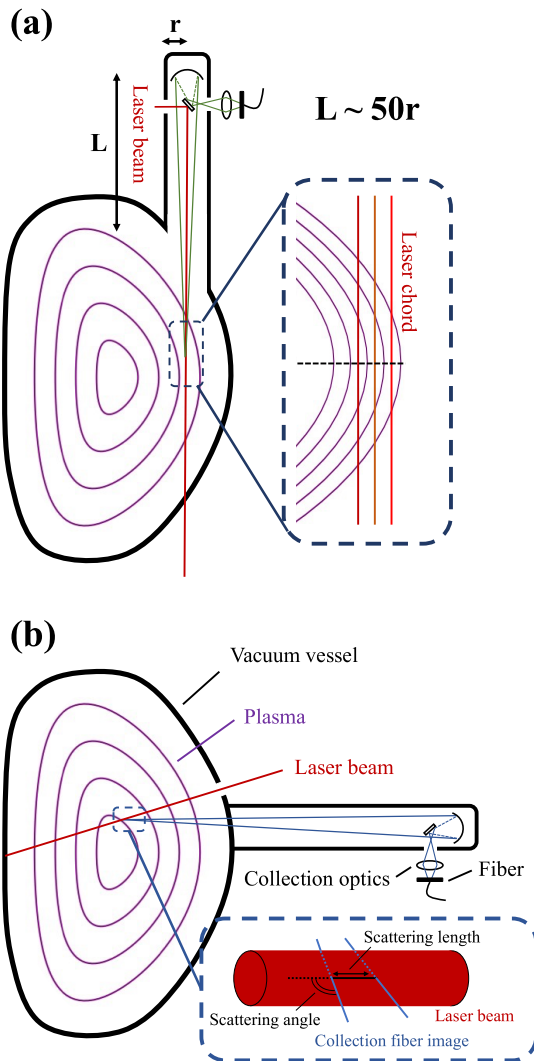Scattering angle   Laser beam

Collection fiber image

Fig. 1   Schematic diagram of (a) a line integrated backward TS system and (b) a standard TS system.

$$T_e(R) = T_{e0} \times \left[\text{Tanh}(2(R_{gT} - R)/R_{wT}) + 1 \right]/2, \quad (2)$$

where n_{e0}, T_{e0} represent pedestal shoulder density and temperature, R represents major radius, $R_{gn} = 10.85$ m and $R_{wn} = 0.12$ m are fixed parameters indicating the steep density gradient position and the density gradient width, respectively. $R_{gT} = 10.85$ m and $R_{wT} = 0.24$ m represent the similar parameters for the temperature. The profile shapes are expressed by similar function as that used in [9], and the above parameters are chosen based on Ref. [10]. The density and temperature at off-midplane position ($Z \neq 0$) is obtained by assuming that the magnetic flux surfaces (We assume equi-density and equi-temperature on the surfaces) are given by

$$R_m(a, \theta) = R_0 + a \cos(\theta + \delta \sin(\theta)), \quad (3)$$
$$Z_m(a, \theta) = \kappa \times a \sin(\theta), \quad (4)$$

$R_0 = 8.5$ m represents plasma major radius, $a = 2.42$ m represents plasma minor radius, $\delta = 0.33$ represents triangularity, $\kappa = 1.65$ represents elongation, θ represents poloidal angle. By adjusting minor radius $a = 0 \sim 2.42$ m, a series of magnetic surfaces are defined, then density and temperature profile at equatorial plane can be extended to off-midplane position.

Figure 2 shows the prepared pedestal profile, in which $n_{e0} = 0.9 \times 10^{20}$ m^{-3} and $T_{e0} = 8$ keV. The measurement major radius range is $R = 10.69 \sim 11.02$ m to cover the whole pedestal region. The first (collection) mirror has roughly the same width ($r = 0.2$ m) as the measurement range. The pedestal width in radial direction is roughly $120 \sim 240$ mm. We set 10 spatial points to be measured in the steep gradient region shown by red dashed lines in Fig. 2, and the target spatial resolution is 12 mm.

Figure 3 (a) shows the schematic drawing of the optical configuration of Fig. 1 (a). The concave mirror is replaced by a thin lens with radius $r_l = 0.2$ m. A fiber with
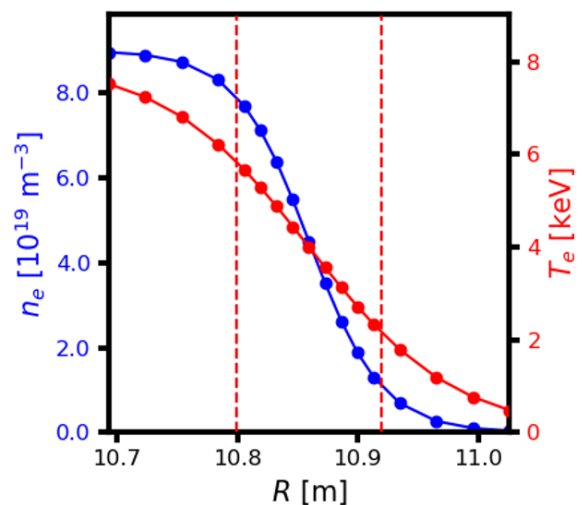

Fig. 2   Target plasma density and temperature profiles. The red dashed lines indicate the high-pressure gradient region.
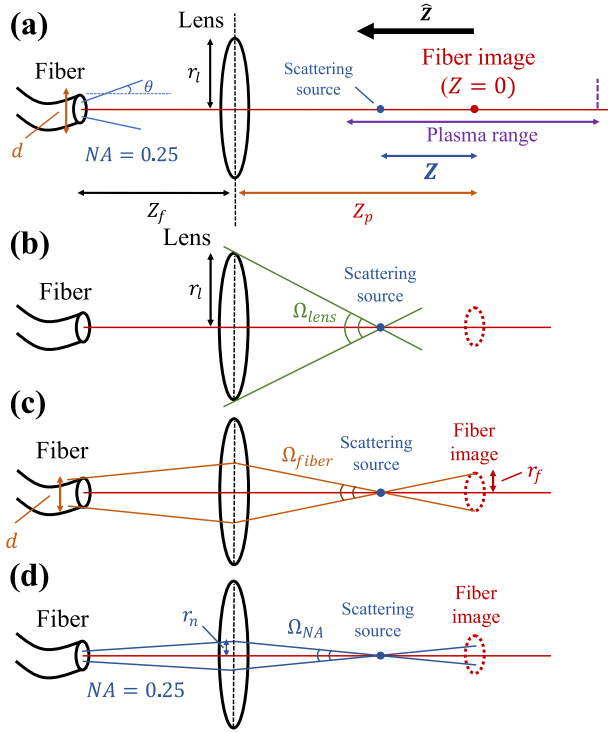
Fig. 3 (a) Schematic diagram of single lens model, (b) lens radius limit Ω_{lens}, (c) fiber radius limit Ω_{fiber} and (d) numerical aperture limit Ω_{NA}.

numerical aperture $NA = 0.25$ and diameter $d = 2\,\text{mm}$ is used [11]. We use the following thin lens formula

$$\frac{1}{f} = \frac{1}{Z_f} + \frac{1}{Z_p},\tag{5}$$

where f is the focal length, Z_f is distance from fiber to lens, Z_p ($= 13\,\text{m}$) is distance from lens to fiber image located at the midplane. The image size is $d \times Z_p/Z_f$.

Based on this single lens model, the sensitivity of collection optics for laser chord is defined as

$$\Delta(R) = \int_{z_{\min}}^{z_{\max}} \Omega(Z)dZ.\tag{6}$$

Where $\Omega(Z)$ is the solid angle profile within the plasma region ($Z_{min} < Z < Z_{max}$), and Z represents the vertical coordinate along the laser beam. Z_{min} and $Z_{\max}$ represents the vertical boundaries of the plasma, and they depend on R. Here we assume $\Omega(Z)$ is independent of R, and all the chords (at different R) has the same optical configuration. This situation can be approximately achieved by tilting the optical components around the center of the collection lens (or concave mirror). The solid angle $\Omega(Z)$ is limited by the following three reasons. (1) The scattering light should hit the collection lens (i.e., concave mirror in the actual configuration), which will limit Ω_{lens} (Fig. 3 (b)), (2) The light should enter the fiber, and this condition is equivalent to the situation that the scattered light (or its straight extension) should pass through the fiber image with size $d \times Z_p/Z_f$

at $Z = 0$, and this condition limits Ω_{fiber} (Fig. 3 (c)), (3) The incident angle of the light entering the fiber should be smaller than the angle determined by NA, this limits Ω_{NA} (Fig. 3 (d)). Then three constraints formula for solid angle are given in following

$$\Omega_{lens} = \frac{\pi r_l^2}{(Z_p - Z)^2} \equiv \frac{A_l^2}{(Z_p - Z)^2},\tag{7}$$

$$\Omega_{fiber} = \frac{\pi r_f^2}{Z^2} \equiv \frac{B^2}{Z^2}, \quad r_f = \frac{d}{2}\frac{Z_p}{Z_f},\tag{8}$$

$$\Omega_{NA} = \frac{\pi r_n^2}{(Z_p - Z)^2} \equiv \frac{A_N^2}{(Z_p - Z)^2},$$

$$r_n = \frac{d}{2} + z_f NA \approx z_f NA.\tag{9}$$

Here we define $A_l^2 \equiv \pi r_l^2$, $B^2 \equiv \pi(dZ_p/2Z_f)^2$ and $A_N^2 \equiv \pi(Z_f NA)^2$ to clarify the derivation shown later. Equations (7), (8) and (9) represent the solid angles spanned by the lens, the fiber image and the numerical aperture projection on lens on scattering source at Z. r_f in Eq. (8) is the fiber image radius. r_n in Eq. (9) is the radius of fiber numerical aperture projection on the lens. The solid angle profile is then given by

$$\Omega(Z) = \min(\Omega_{lens}, \Omega_{fiber}, \Omega_{NA}).\tag{10}$$

Figure 4 (a) shows the solid angle profile calculated at the normalized minor radius $\rho = 0.95$ ($R = 10.79\,\text{m}$), and conditions of Ω_{lens} and Ω_{NA} becomes the same when $r_l/Z_f = NA$ ($Z_f = 0.77\,\text{m}$). Under this situation, the thin lens covers collection cone spanned from fiber, whose size is decided by NA, and sensitivity of collection optics is optimized as described in the following.

In order to evaluate different optical configurations and to find an optimum, we introduce a sensitivity, which is a line integrated solid angle. This is often used to evaluate the efficiency of a Thomson scattering system. The sensitivity is the area of the solid curve shown in Fig. 4 (a). The central region including $Z = 0$ is limited either by Ω_{lens} or Ω_{NA}, and both has the same Z dependences but Z_f dependences are different. To deal both cases we use A to represent either A_l or A_N. The edge region is limited Ω_{fiber}, which depends on Z and Z_f. To obtain the sensitivity we should calculate $Z-$integration at the three regions, which are divided by two intersection points $Z = Z_\pm$ ($Z_+ > 0$, $Z_- < 0$). The actual expressions of $Z_\pm$ depends on which of Ω_{lens} and Ω_{NA} are the limiting condition, and the expressions for $Z_\pm$ ($= Z_{l\pm}$ or $Z_{N\pm}$) are given later. Then the sensitivity is given as

$$\Delta = \int_{Z_-}^{Z_+} \frac{A^2}{(Z_p - Z)^2}dZ + \int_{-L}^{Z_-} \frac{B^2}{Z^2}dZ + \int_{Z_+}^{L} \frac{B^2}{Z^2}dZ$$

$$= A^2 \frac{Z_+ - Z_-}{(Z_p - Z_+)(Z_p - Z_-)} + B^2 \frac{Z_- - Z_+}{Z_+ Z_-} - B^2 \frac{2}{L}$$

$$= -\frac{2B^2}{Z_+ Z_-}(Z_+ - Z_-) - \frac{2B^2}{L} = \frac{4AB}{Z_p} - \frac{2B^2}{L},\tag{11}$$
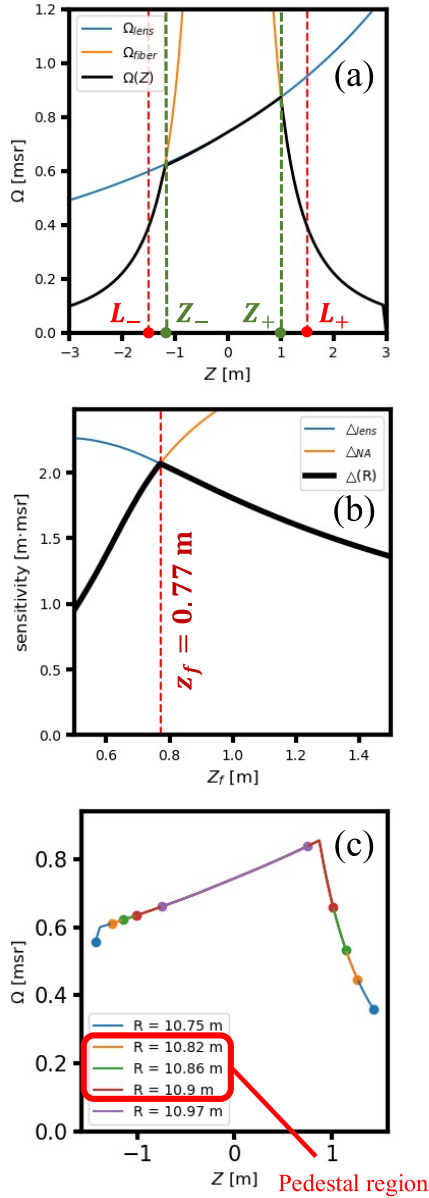
Fig. 4 (a) Solid angle profile along laser path, (b) sensitivity profile under fiber radius and numerical aperture constraint and (c) solid angle profile within pedestal region.

where $\pm L$ are the boundary positions along laser path (Fig. 4 (a) red dash lines). To obtain the final line in Eq. (11) we used the following relationship obtained from the intersection condition Ω_{lens} or $\Omega_{NA} = \Omega_{fiber}$.

$$\frac{A}{Z_p - Z_\pm} = \pm \frac{B}{Z_\pm}, \quad Z_\pm = \pm \frac{B}{A \pm B} Z_p. \tag{12}$$

Using the definition of A_l, A_N, B, we obtain the following sensitivities of Δ_{lens} and Δ_{NA}.

$$\Delta_{lens} = \frac{2\pi r_l d}{Z_f} - \frac{2\pi}{L} \left(\frac{d}{2} \frac{Z_p}{Z_f}\right)^2, \tag{13}$$

$$\Delta_{NA} = 2\pi d NA - \frac{2\pi}{L} \left(\frac{d}{2} \frac{Z_p}{Z_f}\right)^2. \tag{14}$$

We should choose smaller one of these, because it limits the sensitivity, but the choice depends on Z_f as shown in Fig. 4 (b). When we compare Eqs. (13) and (14), the first term of Δ_{lens} is a decreasing function of z_f while that of Δ_{NA} is constant. Both becomes the same as $Z_{f0} = r_l/NA$ ($Z_{f0} = 0.77$ m for the present configuration). If Z_f is smaller than Z_{f0}. $\Delta_{NA} < \Delta_{lens}$, then we should adopt Δ_{NA}. Since Δ_{NA} is the increasing function of Z_f, Z_{f0} yields the highest sensitivity in this region $Z_f < Z_{f0}$. Although Δ_{lens} is a decreasing function of Z_f, such a behavior depends on parameters d, Z_p, L, and a few times difference in one of these parameters can make Δ_{lens} an increasing function of Z_f. We assumed that L is long enough to satisfy $L > |Z_\pm|$, but this is not always true as shown in Fig. 4 (c). Figure 4 (c) shows solid angle profile within plasma range under different radial position R, two boundary points of solid angle profile at each radial position R represent $L_\pm$. At $R = 10.75$ m $L > |Z_\pm|$ is satisfied, in pedestal region $R = 10.82 \sim 10.9$ m $L > |Z_+|$ and $L < |Z_-|$, and at $R = 10.97$ m $L < |Z_\pm|$. We calculated Δ, and then $Z_f = Z_{f0}$ yielded the optimum configuration. The solid angle is not uniform along laser chord, which implies that solid angle will be a weight function in the integration of line-integrated signal. But since solid angle profile is rather flatten instead of peak-like profile, so this measurement is considered as nearly line-integrated measurement.

In the above calculation, the solid angle profile is calculated on optical axis with thin lens formula. In practice the laser beam has a finite beam width, and if a spherical mirror is used to collect the scattering light, then aberration may degrade the solid angle profile. These two factors are discussed in the following.

The finite beam width has most impact on numerical aperture constraint Ω_{NA}. When we take into account this impact, Ω_{NA} is expressed as $\Omega_{NA} = A_{NA}/(Z^2 + Y^2)$, where A_{NA} represents area of overlapped region between fiber image and collection cone of scattering source, and Y represents off-axis distance of scattering source. So as off-axis distance increases, the overlapped region between fiber image and collection cone of scattering source may quickly decrease, which is shown in Fig. 5 (a). A Gaussian beam waist radius of 0.5 mm in plasma pedestal region is feasible, because the beam divergence is 10^{-3} rad (for the wavelength of 1 μm) and the radius at the mirror is about 6.5 mm, which is much smaller than the mirror radius of 200 mm. Figure 5 (b) shows the off-axis effect on the solid angle for off-axis distance of 5 mm. The effect is negligible when the distance is 5 mm, which is an extreme case (beam waist radius of 5 mm, much larger than 0.5 mm case). Therefore, in this research, the solid angle profile will be approximated using on-axis case.

For a spherical mirror, aberration is caused by different focal position of non-paraxial and paraxial incident light. Using the variables defined in Fig. 6 (a), the relationship between a non-paraxial focal length f' and the parax-
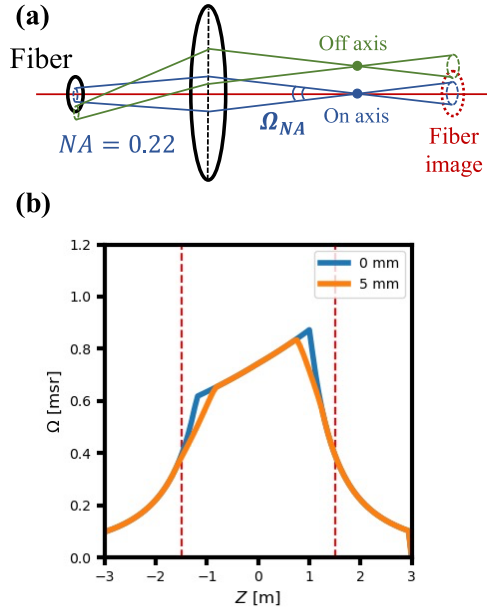
Fig. 5　(a) Schematic diagram of impact of finite beam width, (b) comparison of solid angle profile under different off-axis cases.

ial focal length f is given by

$$f' = 2f - \frac{(2f)^2}{2((2f)^2 - h^2)^{1/2}}, \tag{15}$$

where h is the height of the non-paraxial light. This change in f moves the fiber image position and its effect can be easily calculated for a given h. Then overall solid angle profile is given by

$$\Omega(Z) = \int_0^{h_{max}=0.2} d\Omega(Z, h), \tag{16}$$

$$\Omega(Z, h) = min(\Omega_{lens}(Z), \Omega_{NA}(Z), \Omega_{fiber}(Z, h)), \tag{17}$$

where $d\Omega(Z, h)$ is the contribution of the light hitting the lens at $h \sim h + dh$ to the solid angle. Note that Ω_{lens} and Ω_{NA} become the same at $Z_f = Z_{f0}$. Figure 6 (c) shows the comparison of solid angle profile by assuming paraxial condition and considering aberration effect (on varying the fiber image position). The solid angle profile has no significant distortion within the range $-1\,\mathrm{m} < Z < 1\,\mathrm{m}$. Therefore, in this research paraxial assumption is taken for simplicity.

　　In this section, a single lens model is used to estimate the solid angle profile and sensitivity of collection optics. It is shown that the solid angle profile in pedestal region is nearly line-integrated, and finite beam width and spherical aberration can be neglected in this research. Figure 7 shows the sensitivity profiles within the pedestal region. The sensitivity in the line integrated TS is at least 2 orders of magnitude larger than that of a standard TS due to the extended scattering length, and the sensitivity profile is rather uniform. Here the sensitivity of the standard TS is
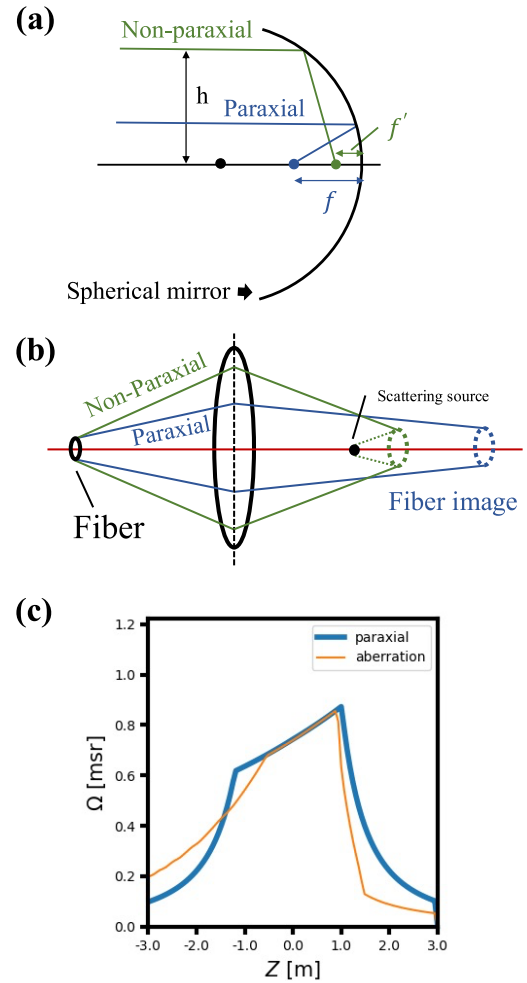

Fig. 6　(a) Schematic diagram of aberration of spherical mirror, (b) schematic diagram of aberration simulated in thin lens model, (c) solid angle profile under paraxial case and non-paraxial (aberration) case.
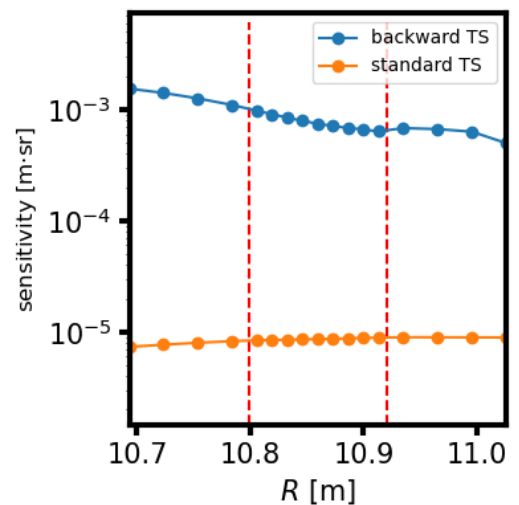

Fig. 7　Comparison of sensitivity profile between line integrated background TS and standard TS configuration.

calculated assuming scattering length is 12 mm to satisfy the requirement on the spatial resolution (of 12 mm).

3. Estimation of Signal Level

Two noise components are considered in this research, (1) Poisson noise and (2) plasma background radiation. In this study, we did not consider the stray light, because the effect depends on the detail of designs. Here, we show several factors which affect the stray light in the proposed system. Compared to the standard TS configurations, the distance between the wall and the measurement point is short (e.g. 1.5 m at the minimum) and it is not easy to distinguish the TS signal and the stray light generated at the wall in time domain (see waveforms in Refs. [12, 13]). In contract, the backward scattering scheme and a relatively high edge temperature (e.g. ~ 1 keV), makes it easier to eliminate the stray light in wavelength domain. The collected photon number from each laser chord is then given as

$$N_{total} = N_p \pm \sqrt{N_p} + N_{back} \pm \sqrt{N_{back}}, \quad (18)$$

where N_p represents Thomson scattering photon number, and N_{back} represents plasma background radiation, for which we assume bremsstrahlung emission. $\sqrt{N_{p\,or\,back}}$ represents the associated Poisson noise (i.e., shot noise), which is expected to be the dominant noise [12]. Figure 8 (a) shows the $R-$profile of detected photon number of the Thomson scattering and related Poisson noise ($\propto \sqrt{N_p}$) component. Thomson scattering photon number N_p is given as

$$N_p = 0.5 N_t \sigma_{TS} \int_{z_{min}(R)}^{z_{max}(R)} \frac{1}{4\pi} O(Z) n_e(Z, R) dZ, \quad (19)$$

$$N_t = \frac{\lambda_{laser} E_{laser}}{2\pi\hbar c}, \quad (20)$$

$$O(Z) = \Omega(Z) \times T \times \eta, \quad (21)$$

N_t represents injected photon number in one single laser pulse, $\sigma_{TS} = 7 \times 10^{-29} \, \text{m}^2$ is Thomson scattering cross section, $\hbar$ is reduced plank constant, c is light speed. We assume a laser with the following parameters: $\lambda_{laser} = 1064$ nm is the laser wavelength, $E_{laser} = 5$ J is the laser energy, $\Delta t = 10$ ns is the pulse width. These parameters are reasonable according to Ref. [14]. $O(Z)$ represents overall sensitivity of the collection optics and other components, such as fiber, and polychromator and detector. $\Omega(Z)$ is the solid angle profile along the laser path, and major radius R dependence of Ω can be neglected, $T = 0.8$ is transmissivity of fiber, $\eta = 0.6$ is a typical quantum efficiency of an avalanche photo diode [15], factor of 0.5 indicates the fact that only shorter wavelength part of the scattered wavelength spectrum is measured.

In this research the main component of the plasma radiation is assumed to be the electron bremsstrahlung,
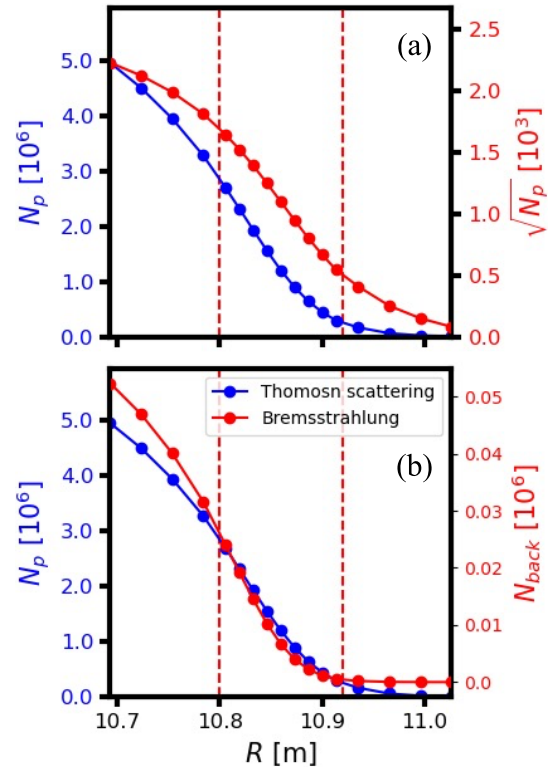

Fig. 8 (a) Comparison of photon numbers of line density of Thomson scattering and Poisson noise. (b) Comparison of photon numbers of line density of Thomson scattering and bremsstrahlung.

whose detected photon number can be approximated as

$$N_{back} = A_f \int \frac{1}{4\pi} O(Z) \frac{dN}{d\nu d\Omega} d\nu dZ, \quad (22)$$

$$\frac{dP}{d\nu d\Omega} = n_e^2 Z_{eff}^2 \left(\frac{e^2}{4\pi\varepsilon_0} \right)^3 \frac{32\pi^2}{3\sqrt{3}m_e^2 c^3} \left(\frac{2m}{\pi T} \right)^{\frac{1}{2}}$$
$$\times \exp\left(-\frac{2\pi\hbar\nu}{T} \right), \quad (23)$$

$$g = \frac{\sqrt{3}}{\pi} K_0 \left(\frac{2\pi\hbar\nu}{2T} \right) \times exp\left(\frac{2\pi\hbar\nu}{2T} \right), \quad (24)$$

$$\frac{dN}{d\nu d\Omega} = \frac{dP}{d\nu d\Omega} \frac{1}{2\pi\hbar\nu} \times \Delta t, \quad (25)$$

where A_f ($= \pi \times (17\text{mm})^2$) is fiber image cross section in midplane for the magnification of Z_p/Z_f, m_e is electron mass, $Z_{eff} = 1.5$ is effective charge in pedestal region, n_e, T_e are plasma density in m^{-3} and temperature in eV, ν is frequency of collected photons. Density and temperature profiles used in Fig. 8 (b) are assumed be the same as the target profiles shown in Fig. 2 ($n_{e0} = 9 \times 10^{19} \, \text{m}^{-3}$, $T_{e0} = 8$ keV).

Figure 8 (b) shows the comparison of detected photons number between Thomson scattering and bremsstrahlung. The latter is negligible and is not considered in the following processes. Note that the bremsstrahlung is proportional to the square of density, and its effect becomes smaller for

a lower density.

4. Reconstruction Method and Noise Performance

Now we will estimate the reconstruction error due to the Poisson noise of Thomson scattering light. We do not evaluate the systematic error arising from the difference between the continuous profiles and discretized profiles, because such systematic error can be corrected by an iterative analysis procedure.

The discrete form of Eq. (19) for k-th line density measurement is

$$N_p(k) = 0.5 N_t \sigma_{TS} \sum_{j=1}^{2k-1} \frac{1}{4\pi} O(j,k) n_e(j) \Delta Z(j,k), \tag{26}$$

in which k represents index of radial layer. $k = 1$ indicates outermost layer, and $k = k_{max}$ indicates innermost layer. j represents index of intersected radial layer along laser path, $\Delta Z(j,k)$ represents length of intersected radial layer. Figure 9 (a) shows three possible laser paths within pedestal region, magnetic surfaces are given by Eqs. (3) and (4). Along single laser path, each radial layer is intersected by laser twice except for innermost layer. When

(a)
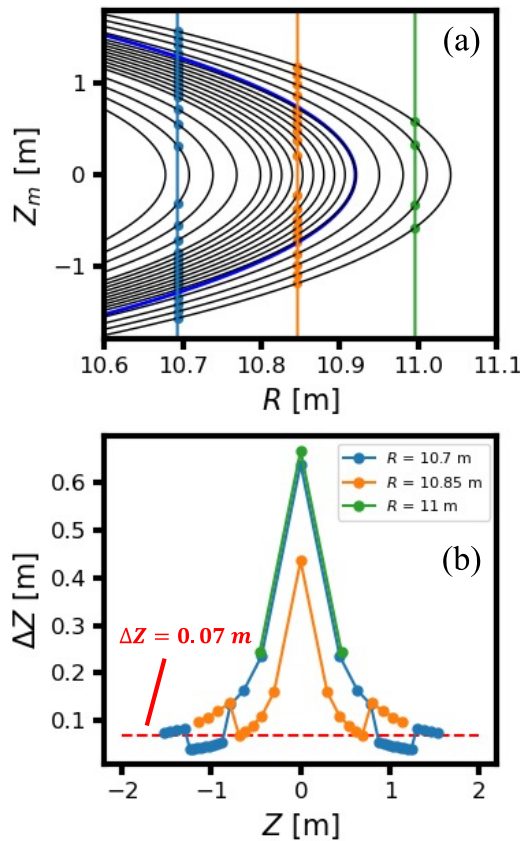
(b)

$\Delta Z = 0.07\ m$

Fig. 9 (a) Cross section of laser path. (b) Path length $\Delta Z(j,k)$ profile under different radial layer. Each dot corresponds to j in Eq. (26), ΔZ for the LIDAR maximum spatial resolution is also shown in red dash line.

we adopt a single chord vertical LIDAR system, $\Delta Z(j,k)$ is the length of scattering volume along Z direction to resolve the signal at each layer. Length of intersected layer of each path $\Delta Z(j,k)$ is shown in Fig. 9 (b), ΔZ for the LIDAR maximum spatial resolution is ~ 70 mm which is shown in red dash line in Fig. 9 (b). With LIDAR system only radial profile with $R \geq 10.85$ m can be resolved by a single chord. From Fig. 9 it is clear that a single chord LIDAR system is not sufficient to resolve the whole pedestal structure, but a multiple chord LIDAR may be an optional method.

Equation (26) can be further simplified by observing that $n_e(j)$ profile along laser path is symmetry to innermost layer. Redefining solid angle $O(j,k)$ and length of intersected layer $\Delta Z(j,k)$ as following

$$O'(j,k) = \begin{cases} O(j,k) + O(2k-j,k), & j=1,2,\ldots,k-1 \\ O(j,k), & j=k \end{cases}, \tag{27}$$

$$\Delta Z'(j,k) = \begin{cases} \Delta Z(j,k) + \Delta Z(2k-j,k), & j=1,\ldots,k-1 \\ \Delta Z(j,k), & j=k \end{cases}. \tag{28}$$

Then Eq. (26) becomes

$$N_p(k) = 0.5 N_t \sigma_{TS} \sum_{j=1}^{k} \frac{1}{4\pi} O'(j,k) n_e(j) \Delta Z'(j,k), \tag{29}$$

Equation (29) can be rewritten as,

$$N_p(k) = \sum_{j=1}^{k} L_{kj} n_e(j), \tag{30}$$

where L_{kj} is kj−element of the matrix L. Then the density profile $n_e(j)$ can be obtained by using an appropriate inverse matrix l as

$$n_e(j) = \sum_{k=1}^{j} l_{jk} N_p(k). \tag{31}$$

The noise of reconstructed density profile due to line density Poisson noise is given by

$$\langle \Delta n_e(j)^2 \rangle = \sum_{k=1}^{j} l_{jk}^2 \langle \Delta N_p(k)^2 \rangle. \tag{32}$$

Here, we use the error propagation formula with the fact that Poisson noise at different lines are independent. $\langle \Delta N_p(k)^2 \rangle = N_p(k)$ is the variance of Poisson noise, Eq. (32) indicates that for a given layer all the noises at outer lines contribute to the density noise at the layer. In this study, we did not consider the effect of error in the magnetic flux surface shapes, which is necessary to calculate l_{jk} in Eq. (32). Since it is difficult to estimate the error presently, we would like to leave it as a future task. For temperature measurement, we assume that line integrated signal at each k-th radial layer is split into multiple wavelength channels to measure the distribution function. To simplify the discussion, two channels are assumed, $N_p(k) = N_p(k, \lambda < \lambda_0) + N_p(k, \lambda > \lambda_0)$, λ_0 represents splitting wavelength position, $N_p(k, \lambda < \lambda_0)$ represents high
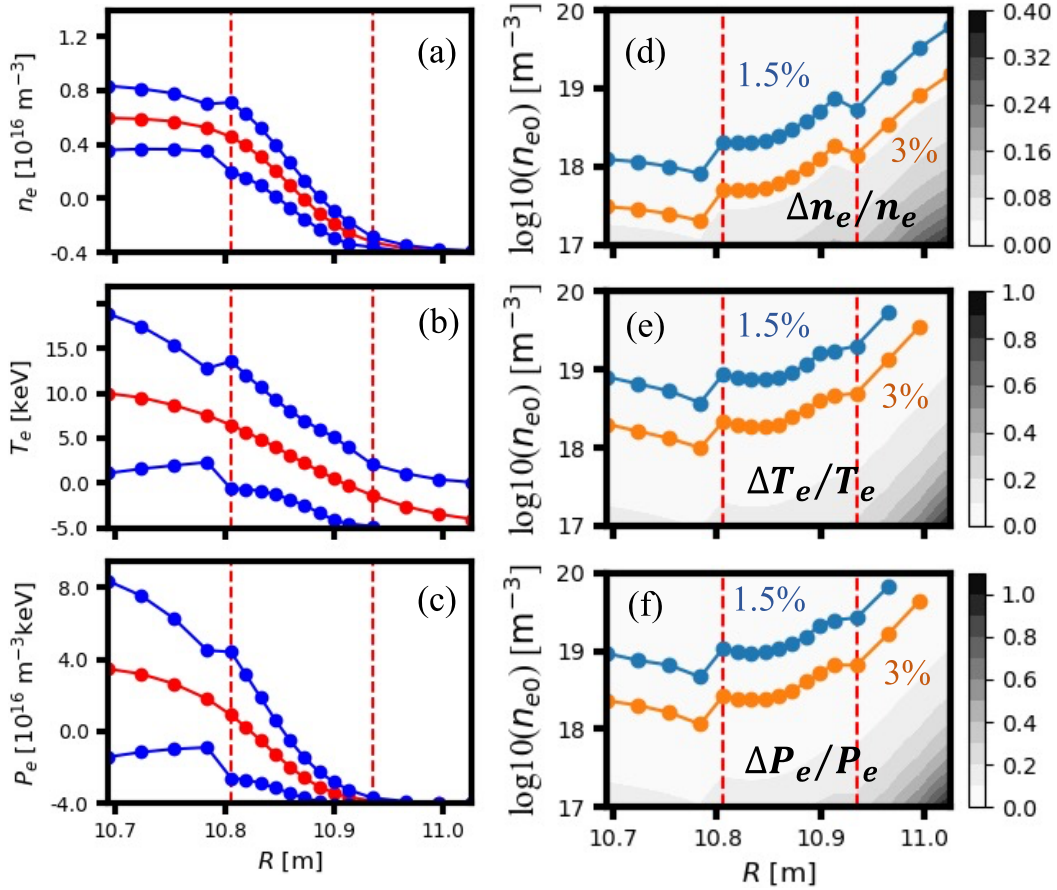
Fig. 10 Reconstructed profile of (a) density, (b) temperature and (c) pressure, and reconstructed noise level of (d) density, (e) temperature and (f) pressure. In (a), (b), (c), red curves represent target n_e, T_e, P_e profiles, dark blue curves represent reconstructed profile with noise $n_e \pm \Delta n_e$, $T_e \pm \Delta T_e$ and $P_e \pm \Delta P_e$. In (d), (e), (f), blue curves represent reconstructed noise profile with noise level 1.5%, orange curves represent reconstructed noise profile with noise level 3%.

velocity component, $N_p(k, \lambda > \lambda_0)$ represents low velocity component. The two lines integrated signals of two channels will be inverted by Eq. (31) to get $n_e(j, \lambda < \lambda_0) \equiv n_h$ and $n_e(j, \lambda > \lambda_0) \equiv n_l$ separately. Then temperature profile can be approximated as following

$$T_e(j) = C(j) \times \frac{n_h}{n_l}, \tag{33}$$

λ_0 is chosen to get the ratio $\langle N_p(k, \lambda < \lambda_0) \rangle / \langle N_p(k, \lambda > \lambda_0) \rangle = 0.23$, by which we obtain a nearly best performance in terms of the noise. The relative error of reconstructed temperature profile is given by

$$\frac{\langle \Delta T_e^2 \rangle}{\langle T_e^2 \rangle} = \frac{\left\langle \Delta \left(\frac{n_h}{n_l} \right)^2 \right\rangle}{\left(\frac{\langle n_h \rangle}{\langle n_l \rangle} \right)^2} = \left[\frac{\langle \Delta n_l^2 \rangle}{\langle n_l \rangle^2} + \frac{\langle \Delta n_h^2 \rangle}{\langle n_h \rangle^2} \right]$$

$$= \left[\frac{1}{\langle n_l \rangle} + \frac{1}{\langle n_h \rangle} \right], \tag{34}$$

in which $\langle \Delta n_{l,h}^2 \rangle$ is the variance of low and high velocity components Poisson noise. $\langle n_{l,h} \rangle$ represents the mean of low and high velocity components.

Figures 10 (a), 10 (b) and 10 (c) show the reconstructed profile at a low shoulder density (5×10^{15} m^{-3})

condition to emphasize Poisson noise effect. Red curve represents target n_e, T_e and P_e profile, blue curves represent reconstructed profile with noise level $n_e \pm \Delta n_e$, $T_e \pm \Delta T_e$ and $P_e \pm \Delta P_e$. The small structures developed around pedestal boundary (red dash line in Fig. 10) is due to the difference in required spatial resolutions in the both sides of boundary which reflects the noise enhancement in reconstruction process (see Eq. (32)). In pedestal region there are more measurement chords which make spatial resolution higher compared to outer region which has less measurement chords. Note that the degree of enhancement increases with the number of chords used in reconstruction process. Figures 10 (d), 10 (e) and 10 (f) show relative noise levels in $R - n_{e0}$ space, where n_{e0} is the shoulder density (at $R = 10.69$ m). Within the density range of interest $10^{19} \sim 10^{20}$ m^{-3} in JA DEMO, the error of the reconstructed profile is within 3% in both density, temperature, and pressure profile. Beside the above described noise accumulation, the relative error decreases with R in the region $R < 10.8$ m and increases with R in the region $R > 10.8$ m. Since the density is nearly flat in the first region, the same noise accumulation causes a higher error for an inner position. In the outer region, however,

the noise accumulation is not serious because the outer region always has lower density. The error in this region is dominated by Poisson noise and the relative error tends to increase with R because of the decreasing density profile. The noise performance of this line integrated measurement satisfies the present criterions of pedestal measurement in ITER, in which noise level of density and temperature profile are 5%, 10% separately for scientific research.

One of practical drawbacks of this scheme is that we need either 20 lasers or vibrating (i.e. tilting) mirror to measure 20 chords.

5. Conclusions

In order to control or avoid ELMs in a fusion reactor, an accurate measurement of pedestal pressure profile is needed. In a reactor, however, the first (collection) mirror should be located far from the plasma to avoid damage on it. Thus, a standard Thomson scattering are believed to be difficult due to the small solid angle of the mirror. We proposed a line-integrated Thomson scattering measurement to achieve a high accuracy by utilizing a long scattering length, while the first (collection) mirror is located behind the tube with length 10 m and radius 0.2 m. Due to the long scattering distance the sensitivity is about 1×10^{-3} m·sr, and this is about 2 orders of magnitude larger than those for a conventional Thomson scattering. Due to the profile reconstruction from line integrated measurements, the error increases, but the resultant error of the reconstructed density, temperature and pressure are at most 1.5%, 3%, 3% separately in pedestal region. The present work demonstrated that a line integrated backward Thomson scattering is feasible and attractive in a fusion reactor.

Acknowledgments

[1] L.L. Lao *et al.*, Nucl. Fusion **41**, 295 (2001).
[2] P.B. Snyder *et al.*, Phys. Plasmas **9**, 2037 (2002).
[3] A.J.H. Donne *et al.*, 'Chapter 7: Diagnostics', Nucl. Fusion **47**, S337 (2007).
[4] W. Biel *et al.*, Fusion Eng. Des. **146**, 465 (2019).
[5] E. Yatsuka *et al.*, JINST **8**, C12001 (2013).
[6] H. Salzmann *et al.*, Rev. Sci. Instrum. **59**, 1451 (1988).
[7] M. Maslov *et al.*, JINST **8**, C11009 (2013).
[8] K. Tobita *et al.*, J. Phys.: Conf. Ser. **1293**, 012078 (2019).
[9] R.J. Groebner and T.N. Carlstrom, Plasma Phys. Control. Fusion **40**, 673 (1998).
[10] R. Sakai *et al.*, Plasma Fusion Res. **15**, 1303031 (2020).
[11] K. Narihara *et al.*, Rev. Sci. Instrum. **72**, 1122 (2001).
[12] A. Ejiri *et al.*, Plasma Fusion Res. **5**, S2082 (2010).
[13] J. Hiratsuka *et al.*, Plasma Fusion Res. **6**, 1202133 (2011).
[14] T. Hatae *et al.*, Rev. Sci. Instrum. **83**, 10E344 (2012).
[15] H. Tojo *et al.*, J. Plasma Fusion Res. SERIES **9**, 288 (2010).